Seasonal and Interannual Variations of the Energy Flux Equator and ITCZ. Part I: Zonally Averaged ITCZ Position

ORI ADAM

ETH Zürich, Zurich, Switzerland

TOBIAS BISCHOFF

California Institute of Technology, Pasadena, California

TAPIO SCHNEIDER

California Institute of Technology, Pasadena, California, and ETH Zürich, Zurich, Switzerland

(Manuscript received 23 July 2015, in final form 4 February 2016)

ABSTRACT

In the zonal mean, the ITCZ lies at the foot of the ascending branch of the tropical mean meridional circulation, close to where the near-surface meridional mass flux vanishes. The ITCZ also lies near the energy flux equator (EFE), where the column-integrated meridional energy flux vanishes. This latter observation makes it possible to relate the ITCZ position to the energy balance, specifically the atmospheric net energy input near the equator and the cross-equatorial energy flux. Here the validity of the resulting relations between the ITCZ position and energetic quantities is examined with reanalysis data for the years 1979–2014. In the reanalysis data, the EFE and ITCZ position indeed covary on time scales of seasons and longer. Consistent with theory, the ITCZ position is proportional to the cross-equatorial atmospheric energy flux and inversely proportional to atmospheric net energy input at the equator. Variations of the cross-equatorial energy flux dominate seasonal variations of the ITCZ position. By contrast, variations of the equatorial net energy input, driven by ocean energy uptake variations, dominate interannual variations of the ITCZ position (e.g., those associated with ENSO).

1. Introduction

Rainfall in the tropics is concentrated in the narrow band of deep convective clouds that marks the intertropical convergence zone (Fig. 1). Paleoclimate records, observations, and simulations of varying complexity indicate that the mean position of the ITCZ and its rainfall intensity vary when the atmospheric energy balance is perturbed, even if the perturbation occurs at distant regions in the extratropics (e.g., Chiang and Bitz 2005; Broccoli et al. 2006; Yoshimori and Broccoli 2008). However, a complete understanding of what drives ITCZ variations on time scales of seasons and longer has remained elusive.

Considering the atmospheric energy balance in the vicinity of the ITCZ has provided some insight into ITCZ shifts, albeit not a complete theory [see Chiang and Friedman (2012) and Schneider et al. (2014) for reviews]. Because the zonal-mean ITCZ lies at the foot of the ascending branch of the tropical Hadley circulation, close to where the near-surface meridional mass flux vanishes, it also lies close to the energy flux equator (EFE), where the column-integrated atmospheric meridional energy flux vanishes (Broccoli et al. 2006; Kang et al. 2008, 2009). Since the Hadley circulation transports energy away from the ITCZ and dominates the atmospheric energy transport (AET) near the equator, the atmospheric energy flux is generally directed southward across the equator when the ITCZ lies north of the equator; conversely, it is directed northward across the equator when the ITCZ lies south of the equator. Indeed, the ITCZ latitude has been found to be negatively correlated with the strength of the cross-equatorial AET in observations and climate simulations (e.g., Kang et al. 2008, 2009; Frierson and Hwang 2012;

Corresponding author address: Ori Adam, Department of Earth Sciences, ETH Zürich, Sonneggstrasse 5, 8092 Zurich, Switzerland. E-mail: ori.adam@live.com

DOI: 10.1175/JCLI-D-15-0512.1

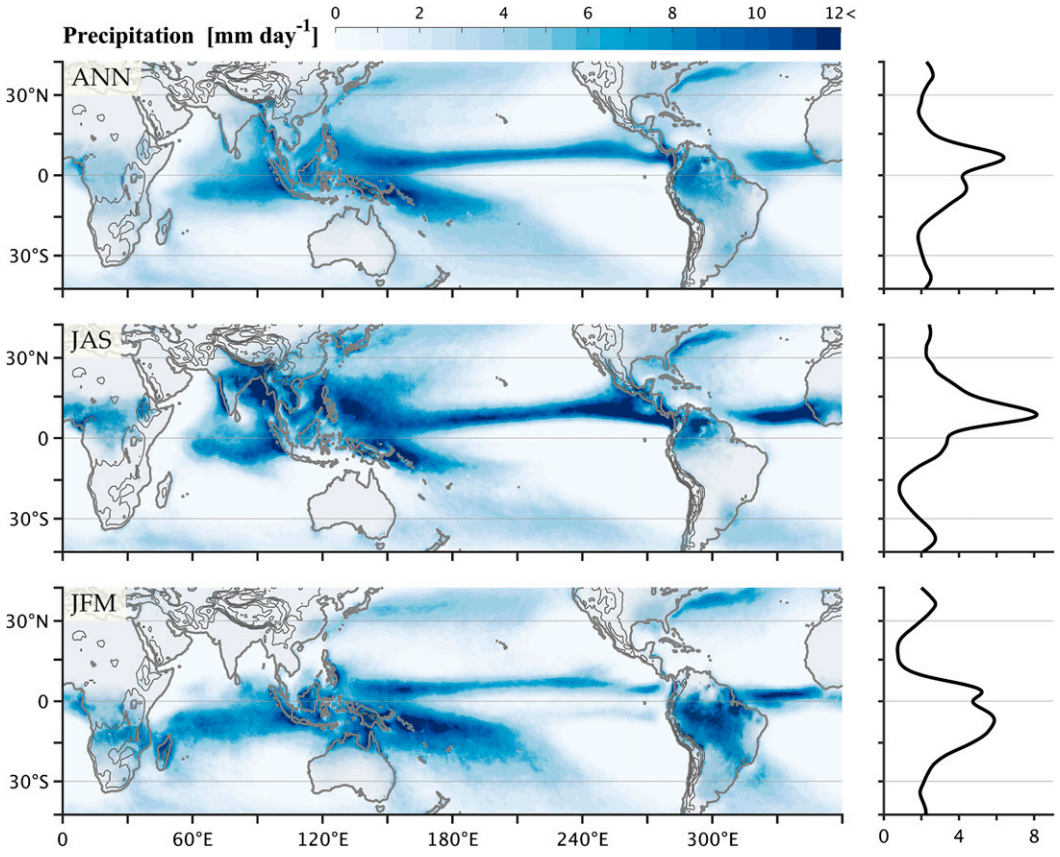

FIG. 1. (left) Annual, boreal summer (JAS), and boreal winter (JFM) mean precipitation (mm day^{-1}). Orography is shown by black contours at 1-km intervals. (right) Zonal-mean precipitation. Data are taken from TRMM for 1998–2014.

Marshall et al. 2014; Frierson et al. 2013; Donohoe et al. 2013, 2014, hereafter D13 and D14, respectively). Theory and simulations with idealized GCMs further suggest that the ITCZ latitude depends on and interacts not only with the cross-equatorial AET but also with the atmospheric net energy input (NEI) near the equator (Bischoff and Schneider 2014, 2016). Variations in NEI likely play a role, for example, when the equatorial eastern Pacific warms under El Niño and the ITCZ shifts equatorward (Fig. 2; Dai and Wigley 2000; Schneider et al. 2014). They may also be responsible for the equatorward ITCZ shift over the western Pacific that has been inferred to have occurred during the Little Ice Age in response to reduced insolation and high aerosol concentrations (Yan et al. 2015). Here we use reanalysis data to examine more closely what kind of energetic perturbations are associated with zonal-mean ITCZ migrations on time scales from seasons to years. We revisit analyses of the association between ITCZ shifts and AET similar to those that have been published previously (D13; D14), adding to those analyses the association between ITCZ shifts and NEI. What emerges is a more nuanced picture of the relation between ITCZ migrations and energetic perturbations, in which the relative importance of AET and NEI variations depends on the time scale considered. After an overview of the data analysis methods we employ (section 2), we briefly summarize the theory underling our analysis (section 3). This is followed by the results of our data analysis (section 4) and a summary and discussion (section 5). This paper focuses on the zonal-mean ITCZ. Extensions to zonally varying aspects of the ITCZ follow in Part II of this study.

2. Data and methods

a. Data sources

We primarily use four-times-daily data at 1.5° horizontal resolution on 37 isobaric levels from the European Centre for Medium-Range Weather Forecasts (ECMWF) interim reanalysis (ERA-Interim, hereafter ERAI) for 1979–2014 (Dee et al. 2011). The data are

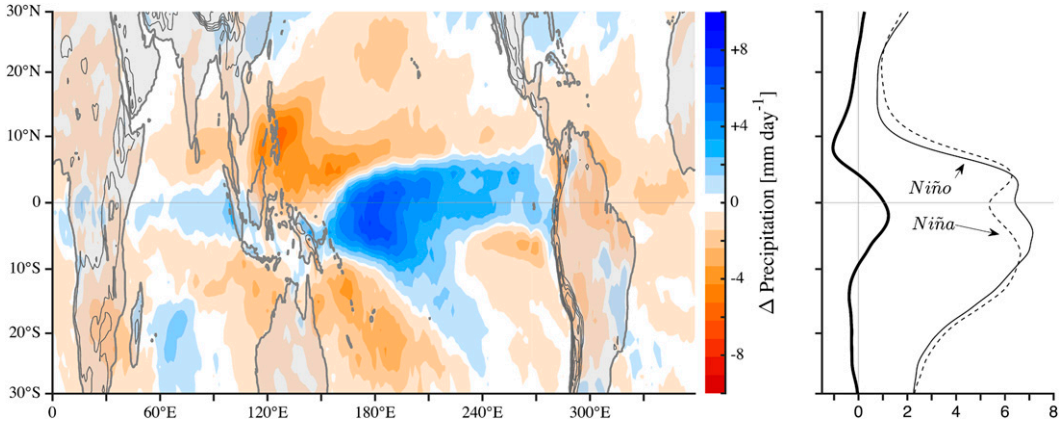

FIG. 2. (left) Boreal winter precipitation (mm day^{-1}) difference between typical El Niño and La Niña conditions. Orography is shown by black contours at 1-km intervals. (right) The zonal mean of the precipitation difference (thick solid) and typical El Niño (thin solid) and La Niña (dashed) conditions. Typical El Niño (La Niña) conditions are defined as ONI values above 0.2 K (below −0.2 K), resulting in a total of 13 El Niño events and 17 La Niña events. Data are taken from ERSST.v3b and ERAI for 1979–2014.

known to have biases, for example, in temperature (Dee and Uppala 2009; Poli et al. 2010) and precipitation (Dee et al. 2011). These biases are not expected to qualitatively affect the large-scale ITCZ position and column-integrated energy fluxes on which we focus here.

For quality control, we compare the ERAI results with results obtained from the following:

1) Tropical Rainfall Measuring Mission (TRMM) Multisatellite Precipitation Analysis (Liu et al. 2012, their Fig. 1) for 1998–2014,
2) National Centers for Environmental Prediction (NCEP)–National Center for Atmospheric Research (NCAR) reanalysis (Kalnay et al. 1996) for 1979–2014,
3) National Oceanic and Atmospheric Administration (NOAA)/Climate Prediction Center (CPC) Merged Analysis of Precipitation (CMAP; Xie and Arkin 1996) for 1979–2014 (obtained from the NOAA/ESRL Physical Sciences Division website http://www.esrl.noaa.gov/psd/),
4) NOAA's Global Precipitation Climatology Project (GPCP) data, version 2.2 (Adler et al. 2003), for 1979–2014, and
5) Clouds and the Earth's Radiant Energy System (CERES) Energy Balanced and Filled (EBAF) data (Wielicki et al. 1996).

Inferring terms in the energy balances from reanalysis data can be problematic because the reanalysis energy balances are not closed. The errors in the column-integrated energy budgets of the ERAI and NCEP–NCAR data are greatest over land, in particular near high topography (Trenberth et al. 2001). In situ measurements indicate that the net shortwave fluxes are the largest source of uncertainties and errors (e.g., Curry et al. 1999), causing local biases that can exceed 30 W m^{-2} in ERAI (Trenberth et al. 2001). Our focus here is on zonal-mean quantities. The estimated bias in the zonal-mean annually averaged column-integrated cross-equatorial flux is around 0.2 PW, although the actual uncertainty is poorly known (Fasullo and Trenberth 2008). This is small compared with seasonal variations, but it does affect the interpretation of interannual variations. To identify El Niño and La Niña episodes, we use the oceanic Niño index (ONI), which is the deviation of the 3-month running mean SST from a moving 30-yr climatology in the Niño-3.4 region. The ONI data were obtained from version 3b of the Extended Reconstructed Sea Surface Temperature (ERSST.v3b) dataset, provided by NOAA's National Climatic Data Center (Smith et al. 2008).

b. Data processing

Data retrieval and analysis were performed using the geophysical observation analysis tool (GOAT), a MATLAB-based tool for geophysical data management (www.goat-geo.org). Statistics needed in our analyses were computed as follows:

1) To compute atmospheric energy fluxes, a barotropic mass flux correction was added to column-integrated fluxes, to ensure that mass budgets are closed. We followed the procedure outlined in Trenberth (1997; documented in detail at www.cgd.ucar.edu/cas/catalog/newbudgets/). Monthly means of the corrected fluxes presented here, computed from the coarse-grained ERAI data on pressure coordinate levels, were found to be in agreement with those produced using data on the native ERAI model grids (Fasullo and Trenberth 2008).

2) The tropopause height was determined using a threshold lapse rate of $2\,\mathrm{K\,km^{-1}}$, as in Reichler et al. (2003).
3) The poleward edges of the Hadley cells and the separator between the Hadley cells at the ITCZ were determined as the tropical zeros of the meridional mass streamfunction, averaged between 300 and 700 mb (1 mb = 1 hPa) and linearly interpolated to 0.1° horizontal resolution.
4) Various indices of the ITCZ latitude were calculated as expected latitudes, using as weighting function an integer power N of the area-weighted precipitation P integrated between the latitudes ϕ_1 and ϕ_2:

$$\phi_E = \frac{\int_{\phi_1}^{\phi_2} \phi[\cos(\phi)P]^N \, d\phi}{\int_{\phi_1}^{\phi_2} [\cos(\phi)P]^N \, d\phi}. \tag{1a}$$

Different ITCZ latitude indices result from different choices of ϕ_1, ϕ_2, and N:

$$\begin{aligned} &\phi_{\max}\{N = 10,\ \phi_1 = 20°\mathrm{S}, \quad \text{and} \quad \phi_2 = 20°\mathrm{N} \\ &\phi_{\mathrm{cent}}\{N = 1,\ \phi_1 = 20°\mathrm{S}, \quad \text{and} \quad \phi_2 = 20°\mathrm{N} \\ &\phi_{\mathrm{SH}}\{N = 10,\ \phi_1 = 20°\mathrm{S}, \quad \text{and} \quad \phi_2 = 0° \\ &\phi_{\mathrm{NH}}\{N = 10,\ \phi_1 = 0°, \quad \text{and} \quad \phi_2 = 20°\mathrm{N}. \end{aligned} \tag{1b}$$

High exponents N yield latitudes close to the precipitation maximum; in practice, we found $N = 10$ to reliably identify the maximum while smoothing some of the discretization noise that would arise when the maximum is directly identified. Thus, $\phi_{\max}$ is the latitude of the tropical precipitation maximum, ϕ_{cent} is the tropical precipitation centroid, and ϕ_{SH} and ϕ_{NH} are the latitudes of the tropical precipitation maxima in the SH and NH, respectively. The term precipitation centroid has been used in some previous papers (Frierson and Hwang 2012; D13; D14) to describe an approximate precipitation median ϕ_{med} (A. Donohoe 2015, personal communication), determined such that

$$\int_{\phi_1}^{\phi_{\mathrm{med}}} \cos(\phi)P \, d\phi = \int_{\phi_{\mathrm{med}}}^{\phi_2} \cos(\phi)P \, d\phi. \tag{1c}$$

This precipitation median ϕ_{med} (with $\phi_1 = 20°$S and $\phi_2 = 20°$N and interpolating precipitation to 0.05° resolution to reduce grid dependence) and the precipitation centroid ϕ_{cent} are closely related in the ERAI, NCEP–NCAR, GPCP, and CMAP datasets. The Pearson correlation coefficient between ϕ_{med} and ϕ_{cent} is greater than 0.99 for monthly variations and greater than 0.9 for interannual correlations. Nonetheless, the monthly variance of ϕ_{med} ranges from latitude 15.6° to 22.7°, whereas the monthly variance of ϕ_{cent} ranges from latitude 9.5° to 13.1°. We focus on results for ϕ_{med} in our analyses; they are usually statistically indistinguishable from those for ϕ_{cent}.

3. Theory

The theory underlying our analysis is that described by Bischoff and Schneider (2014, 2016) and Schneider et al. (2014). Here we provide a brief summary.

The position of the ITCZ is related to the cross-equatorial AET by associating it with the rising branch of the tropical Hadley circulation. In the rising branch of the Hadley circulation, the moist static energy (MSE) of the diverging air aloft is greater than that of the converging air near the surface because MSE generally increases with altitude. Therefore, the column-integrated energy transport across the equator is in the direction of the upper branch of the Hadley circulation, provided eddy energy transport in the deep tropics can be neglected (Neelin and Held 1987; Kang et al. 2009). It follows that an ITCZ located north of the equator implies southward energy flux across the equator, and vice versa.

The MSE is given by

$$h = c_p T + g\Phi + Lq, \tag{2}$$

where the parameters c_p, g, and L denote the specific heat at constant pressure, the gravitational acceleration, and the latent heat of vaporization, respectively, all taken to be constant. The variables T, Φ, and q denote temperature, geopotential, and specific humidity, respectively. The column-integrated energy balance of the atmosphere can be written as follows (e.g., Peixoto and Oort 1992):

$$\partial_t \langle e \rangle + \nabla \cdot \langle \mathbf{u}h \rangle = I + \varepsilon. \tag{3}$$

Angle brackets denote the mass-weighted vertical integral over atmospheric columns. On the left-hand side, e denotes moist enthalpy (MSE minus geopotential energy), t denotes time, and $\mathbf{u} = (u, v, w)$ is the three-dimensional wind vector. On the right-hand side, I denotes the atmospheric NEI, and ε denotes residuals resulting from errors in reanalysis data. The NEI is composed of the net downward shortwave radiative energy flux minus the outgoing longwave radiative energy flux at the top of the atmosphere (TOA) and sensible and latent surface heat fluxes and net upward radiative energy fluxes at the surface. Since the continental heat capacity is relatively small, land heat uptake can generally be neglected. A net energy flux into or out of the surface is therefore primarily associated with

ocean heat storage or ocean energy transport. In the zonal mean, the energy balance becomes

$$\partial_t \langle [e] \rangle + \partial_y \langle [vh] \rangle = [I] + [\varepsilon], \tag{4}$$

where $[\cdot]$ denotes the zonal mean. For simplicity, we use local Cartesian coordinates to denote spatial derivatives, with the meridional distance coordinate given by $y = a\phi$, where a is Earth's radius and ϕ denotes latitude; however, we perform all calculations in spherical coordinates.

By expanding the zonally averaged energy flux around the equator to first order in latitude, and assuming it vanishes at the ITCZ (i.e., the ITCZ lies at the EFE), one obtains the following (Bischoff and Schneider 2014):

$$\widetilde{\phi_I} = -\frac{1}{a}\frac{\langle [vh] \rangle_0}{\partial_y \langle [vh] \rangle_0} = -\frac{1}{a}\frac{\langle [vh] \rangle_0}{[I_0] + [\varepsilon_0] + \partial_t \langle [e] \rangle_0}, \tag{5a}$$

where $\widetilde{\phi_I}$ denotes the ITCZ latitude and the subscript 0 denotes equatorial values. Neglecting ε, in a statistically steady state Eq. (5a) becomes

$$\phi_I = -\frac{1}{a}\frac{\langle [vh] \rangle_0}{[I_0]}. \tag{5b}$$

Thus, to first order in latitude, this energetic framework relates the zonal-mean ITCZ latitude to the cross-equatorial AET $\langle [vh] \rangle_0$ and the inverse of equatorial NEI $[I_0]$ (Bischoff and Schneider 2014).

4. Results

a. Seasonal cycle

The zonal-mean meridional MSE flux can be decomposed into mean meridional circulation (MMC), stationary eddy, and transient eddy components (e.g., Peixoto and Oort 1992):

$$\langle \overline{[vh]} \rangle = \underbrace{\langle [\overline{v}][\overline{h}] \rangle}_{\text{MMC}} + \underbrace{\langle [\overline{v}^*\overline{h}^*] \rangle}_{\text{stationary eddies}} + \underbrace{\langle \overline{[v'h']} \rangle}_{\text{transient eddies}}, \tag{6}$$

where an asterisk denotes deviations from the zonal mean $[\cdot]$, and the overbar and prime denote the time mean and deviations therefrom. If MSE transport by eddies in the deep tropics is small and, if the MSE flux convergence near the surface and divergence aloft are vertically aligned, then we expect the EFE to be collocated with the rising branch of the mean meridional circulation (e.g., Kang et al. 2009).

Figures 3a, 3c, and 3e show latitude–pressure sections of the MMC component of the zonal-mean

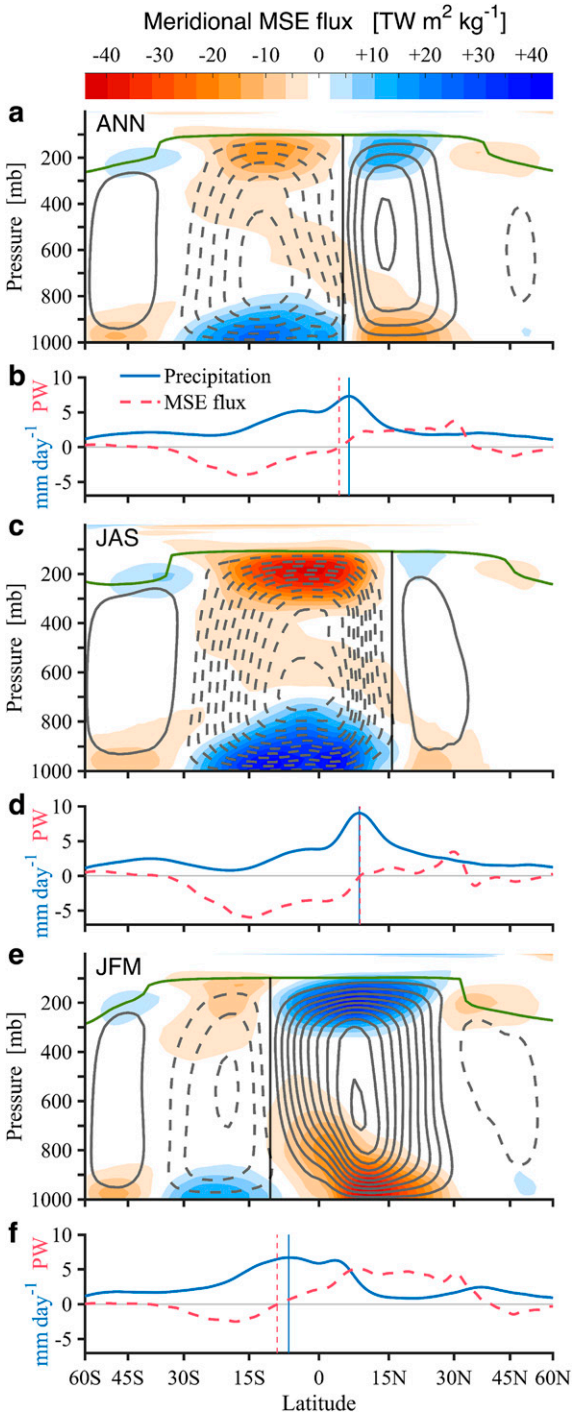

FIG. 3. Latitude–pressure section of the zonal-mean mass streamfunction (contours) and the MMC component of the meridional MSE flux (colors): (a) ANN, (c) JAS, and (d) JFM mean. Solid (dashed) contours indicate positive (negative) values, with a 20-Sv ($1\ \text{Sv} \equiv 10^6\ \text{m}^3\ \text{s}^{-1} \approx 10^9\ \text{kg}\ \text{s}^{-1}$) contour interval. The vertical lines indicate the separator between the two Hadley cells. The tropopause height is shown in solid green. (b),(e),(f) Corresponding zonal-mean precipitation (solid blue) and column-integrated MMC component of the meridional MSE flux (dashed red), with positions of the precipitation maxima (solid blue) and EFEs (dashed red) indicated by vertical lines. Data are taken from ERAI for 1979–2014.

meridional MSE flux (color contours), averaged annually (ANN), over July–September (JAS) and over January–March (JFM), respectively, with superimposed contour lines of the meridional mass streamfunction and tropopause height. (The vertically resolved MSE flux is shown without the mass-flux correction that is applied to column integrals.) The zonal-mean precipitation and column integrals of the MMC components of the meridional MSE flux are shown in Figs. 3b,d,f.

The EFE of the mean component of the circulation, the separator between the two Hadley cells, and the ITCZ (indicated by vertical lines) are generally close to each other but do not exactly covary. The zonal-mean ITCZ latitude (i.e., the precipitation maximum) is 2° poleward of the EFE in the annual mean and 2.5° equatorward of it during JFM (when the zonally averaged SH precipitation distribution is also broadened by the elongated South Pacific convergence zone; see Fig. 1). During JAS, the EFE and ITCZ are exactly collocated, but they lie about 5° equatorward of the Hadley cell separator. The mean-circulation EFE deviates from the Hadley cell separator primarily because the converging MSE fluxes near the surface are not vertically aligned with the diverging fluxes aloft. In addition, although small compared with tropospheric fluxes, stratospheric MSE fluxes can be significant compared with the residual of the vertically integrated tropospheric fluxes (cf. Hill et al. 2015); thus, they can also affect the EFE position.

Figure 4 shows the daily climatology of the column-integrated meridional MSE flux (Fig. 4a) and its MMC (Fig. 4b), stationary eddy (Fig. 4c), and transient eddy components (Fig. 4d). (The stationary component computed from the daily climatology can include some transient influences.) The right panels show the means of the daily climatology. Black lines show the poleward edges and separator of the Hadley cells. As in Fig. 3, the seasonally varying $\phi_{\max}$ (red line) lies equatorward of the Hadley cell separator in the summer hemisphere, for the reasons discussed in D13. Stationary eddy (Fig. 4c) and transient eddy (Fig. 4d) MSE fluxes near the equator are small throughout the year, compared with the MMC component. As a result, the zeros of the total MSE flux and its MMC component do not differ qualitatively. Therefore, for simplicity, we use the zero of the total MSE flux in what follows to determine the EFE in all calculations.

Since tropical overturning and radiative relaxation time scales are of the order of several weeks (Peixoto and Oort 1992), the EFE is not expected to be related to the ITCZ position and Hadley cell separator on subseasonal time scales. Similarly, the typical response times of the ITCZ position and EFE to the seasonally varying forcing may differ. Indeed, variations in EFE

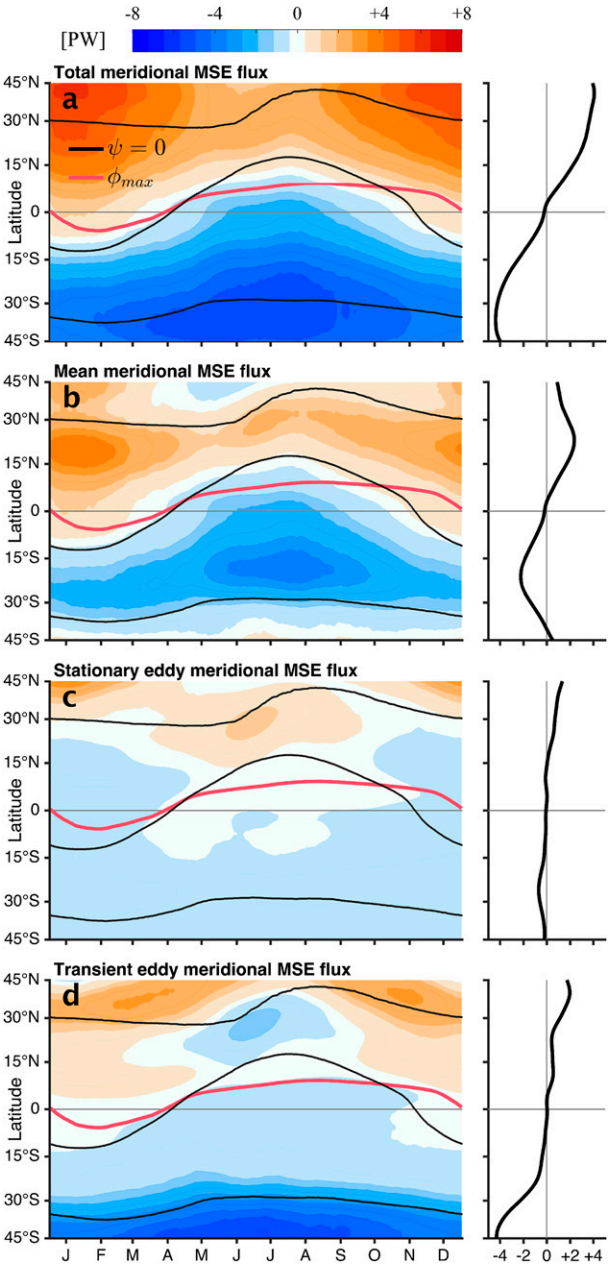

FIG. 4. (left) Daily climatology of column-integrated meridional MSE flux components: (a) total column-integrated MSE flux, (b) mean meridional circulation component, (c) stationary eddy component, and (d) transient eddy component. The tropical zeros of the meridional streamfunction ($\psi = 0$) are shown as black lines and mark the separator between the Hadley cells (middle line) and their poleward edges (outer lines). The precipitation maxima $\phi_{\max}$ are shown in solid red. (right) Annual means of the daily climatology. Data are taken from ERAI for 1979–2014 and are smoothed using a 31-day running mean.

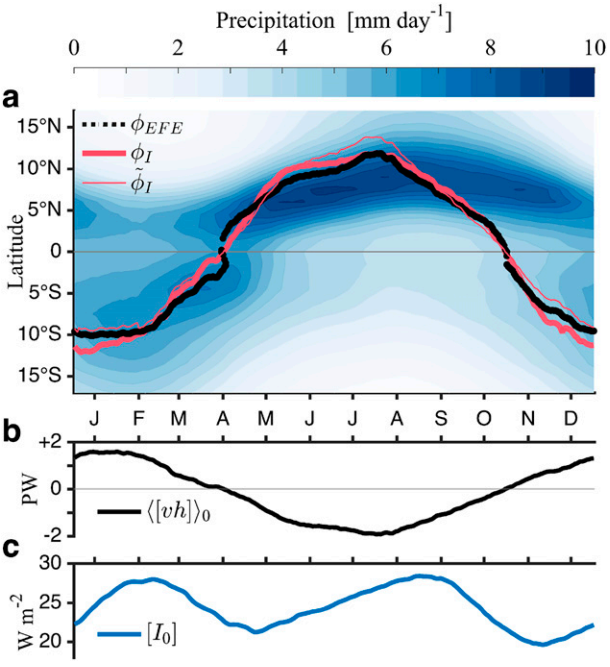

FIG. 5. (a) Daily climatology of zonal-mean area-weighted precipitation (colors). Dotted black line indicates EFE latitude ϕ_{EFE}. Thin red line indicates first-order approximation of the EFE latitude Eq. (5a). Thick red line indicates statistically steady-state approximation Eq. (5b). (b) Cross-equatorial AET $\langle[vh]\rangle_0$ averaged between 5°S and 5°N. (c) Atmospheric NEI $[I_0]$ calculated from TOA and surface energy fluxes and averaged between 10°S and 10°N. Data are taken from ERAI for 1979–2014 and are smoothed using a 31-day running mean.

and ITCZ position are maximally correlated for the ITCZ position (identified as the precipitation maximum) lagging the EFE by 5 weeks.

Figure 5a shows the daily climatology of the EFE latitude ϕ_{EFE} (black), its approximation $\widetilde{\phi_I}$ obtained from Eq. (5a) (thin red), and its approximation ϕ_I obtained from Eq. (5b) under the additional assumption of a statistically steady state (thick red), all overlaid on the zonal-mean area-weighted precipitation. The agreement between $\widetilde{\phi_I}$ and the EFE indicates that the linear approximation [Eq. (5b)] is indeed justified for the zonally averaged ITCZ position. By comparing the annual means of $\widetilde{\phi_I}$ and ϕ_I and by explicitly calculating atmospheric energy storage $\partial_t\langle[e]\rangle_0$, we find that the difference between $\widetilde{\phi_I}$ and ϕ_I is primarily indicative of uncertainty in the reanalyzed data (ε) and to a lesser degree (less than 10% of the difference) due to atmospheric energy storage. Figures 5b and 5c show the daily climatologies of the cross-equatorial AET $\langle[vh]\rangle_0$ and the NEI $[I_0]$, respectively. The subscript 0 denotes values averaged between 5°S and 5°N for $\langle[vh]\rangle_0$ and between 10°S and10°N for $[I_0]$. The results are not qualitatively sensitive to the width of the equatorial averaging boundaries.

The cross-equatorial AET $\langle[vh]\rangle_0$ varies sinusoidally from positive values during boreal winter to negative values during boreal summer. NEI is positive throughout the year and peaks around the equinoxes, modulating the seasonal variations of ϕ_I and $\widetilde{\phi_I}$ by approximately 20%. The ratio of $\langle[vh]\rangle_0$ and $[I_0]$ therefore varies nonlinearly, capturing the swift transitions of the ITCZ across the equator during transition seasons. As already seen in Chiang and Friedman (2012), the maximal discrepancy between the EFE and ITCZ position is observed during boreal autumn, when the lag between the southward shift of the ITCZ and the EFE is about 2 months. This extended lag exists over the Pacific but not elsewhere; it is examined more closely in Part II of this study.

Thus, while it is clear that the seasonal variations of the EFE and its approximations $\widetilde{\phi_I}$ and ϕ_I from the energy balance do not capture the seasonal ITCZ shifts completely, they do have similar amplitude and capture some aspects of the seasonal transitions. Table 1 summarizes the correlations between the various ITCZ latitude indices, the latitude of the energy flux equator ϕ_{EFE}, its approximation ϕ_I, and the energetic quantities $\langle[vh]\rangle_0$ and $[I_0]$ on which the EFE approximation depends. It is clear that it is primarily the cross-equatorial AET $\langle[vh]\rangle_0$ that drives seasonal variations of the approximate energy flux equator ϕ_I.

TABLE 1. Pearson correlation coefficient between the zonal-mean ITCZ latitude indices ϕ_{med}, ϕ_{SH}, and ϕ_{NH} [Eqs. (1a)–(1c)] and the energy flux equator ϕ_{EFE}, its approximation ϕ_I, the cross-equatorial AET $\langle[vh]\rangle_0$, and the equatorial NEI $[I_0]$. Correlations are shown for seasonal (Fig. 5) and interannual variations (Fig. 6), the latter separately for ANN, JAS, and JFM averages. For the interannual correlations, correlations with the ONI are also included. Statistically significant correlations ($p < 0.05$) are highlighted in boldface. Data are taken from ERSST.v3b and ERAI for 1979–2014.

	Seasonal				Interannual					Interannual JAS					Interannual JFM				
	ϕ_{EFE}	ϕ_{med}	ϕ_{SH}	ϕ_{NH}	ϕ_{EFE}	ϕ_{med}	ϕ_{SH}	ϕ_{NH}	ONI	ϕ_{EFE}	ϕ_{med}	ϕ_{SH}	ϕ_{NH}	ONI	ϕ_{EFE}	ϕ_{med}	ϕ_{SH}	ϕ_{NH}	ONI
ϕ_{EFE}	—	**0.87**	**0.92**	**0.73**	—	0.18	−0.04	**0.56**	−0.10	—	−0.19	−0.18	**0.50**	−0.23	—	−0.03	**0.57**	**−0.52**	**0.63**
ϕ_I	**0.99**	**0.84**	**0.92**	**0.70**	**0.72**	0.26	−0.10	**0.40**	0.01	0.28	**0.50**	**−0.42**	**0.53**	−0.13	**0.60**	−0.12	0.19	−0.18	0.30
$\langle[vh]\rangle_0$	**−0.99**	**−0.87**	**−0.94**	**−0.75**	**−0.83**	−0.12	0.12	**−0.41**	−0.05	**−0.64**	0.30	**0.41**	**−0.40**	0.24	**−0.56**	−0.33	−0.29	0.00	−0.06
$[I_0]$	**0.21**	**0.10**	−0.08	0.08	**−0.50**	−0.13	0.10	**−0.54**	0.23	**−0.50**	−0.12	0.20	**−0.53**	0.14	**0.73**	**−0.34**	**0.43**	**−0.70**	**0.68**

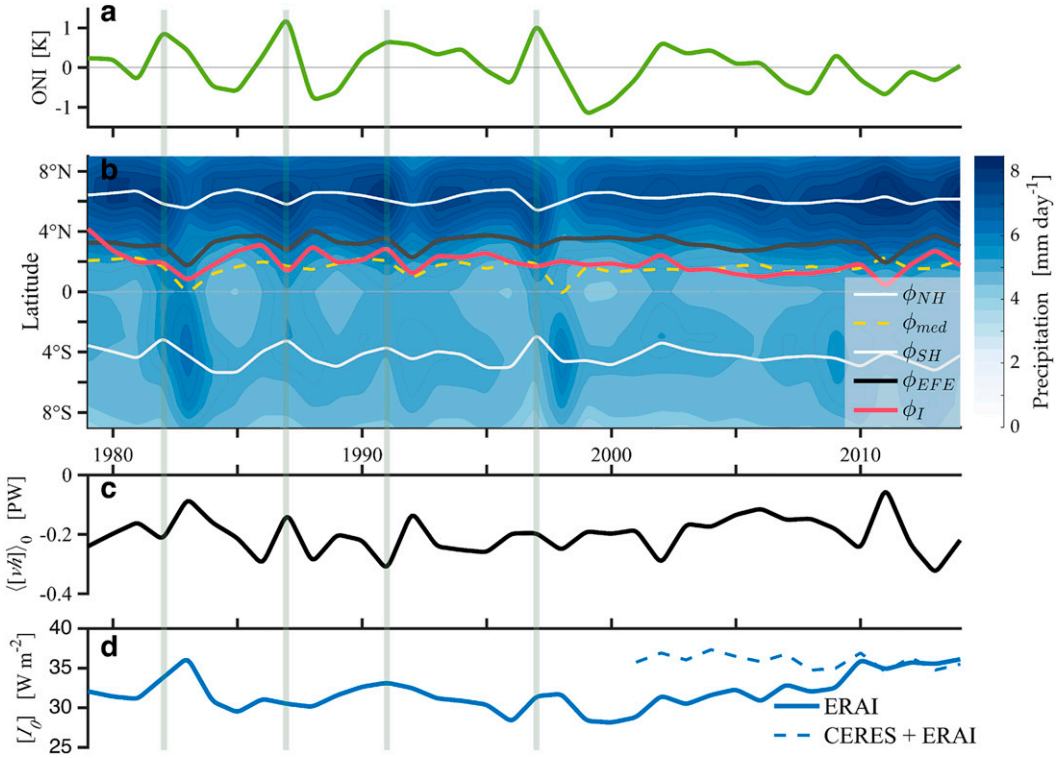

FIG. 6. Interannual variability of ITCZ position and correlates. (a) Annually averaged ONI. (b) Zonal-mean area-weighted precipitation (colors), zonal-mean ITCZ latitude indices ϕ_{med}, ϕ_{NH}, and ϕ_{SH} [Eqs. (1a)–(1c)], as well as energy flux equator ϕ_{EFE} and its approximation ϕ_I. (c) Cross-equatorial AET $\langle[vh]\rangle_0$ averaged between 5°S and 5°N. (d) Equatorial NEI $[I_0]$ averaged between 10°S and 10°N. The four largest peaks of El Niño episodes are indicated by vertical lines. Data are taken from ERSST.v3b and ERAI for 1979–2014.

b. *Interannual variations*

Figure 6 shows how the ITCZ latitude and its correlates (EFE, $\langle[vh]\rangle_0$, $[I_0]$, and the various ITCZ latitude indices) vary interannually. Correlations between ϕ_{EFE}, ϕ_I, $\langle[vh]\rangle_0$, and $[I_0]$ with the three ITCZ position indices and the ONI are summarized in Table 1, separately for annual, JAS, and JFM averages. Phase lags between ONI variations and the ITCZ latitude were found to have a negligible effect on the interannual correlations shown in Table 1. Interannual means of the NEI were calculated as the divergence of the column-integrated energy flux [i.e., neglecting energy storage in Eq. (3)]. These annual means were found to be in better agreement with NEI calculated using radiative fluxes from the CERES dataset (Fig. 6d) than NEI calculated directly from the TOA and surface fluxes of the ERAI dataset.

Extremal values of cross-equatorial AET $\langle[vh]\rangle_0$ are observed during some peak ENSO years. However, variations of $\langle[vh]\rangle_0$ and ONI are not consistently correlated (e.g., compare the highlighted El Niño episodes in 1982 and 1987), resulting in an overall low correlation ($R < 0.25$ for annual, JAS, and JFM means). In contrast, the equatorial NEI $[I_0]$ covaries with ONI because of the decreased ocean heat uptake during El Niño episodes and the increased uptake during La Niña episodes; TOA longwave and shortwave radiative flux variations approximately balance, and their net effect on ENSO-related NEI variations is small (Fig. 7). Variations of equatorial NEI are a significant driver of interannual ITCZ migrations during JFM (when ENSO anomalies are maximal). However, like the $\langle[vh]\rangle_0$ variations, NEI variations are only weakly correlated with the ITCZ latitude in JAS and in the annual mean because the interannual ITCZ migrations are relatively small.

c. *Interannual regressions*

As in D14, interannual correlations calculated using a 1-yr low-pass filter are generally larger, but they are statistically similar to those obtained using annual means. However, our results differ from those of D14, who showed statistically significant interannual correlations between $\langle[vh]\rangle_0$ and ϕ_{med} in reanalysis data and simulations. To test the robustness of our results, we calculated the interannual correlation between $\langle[vh]\rangle_0$ and ϕ_{med} using all possible combinations of $\langle[vh]\rangle_0$

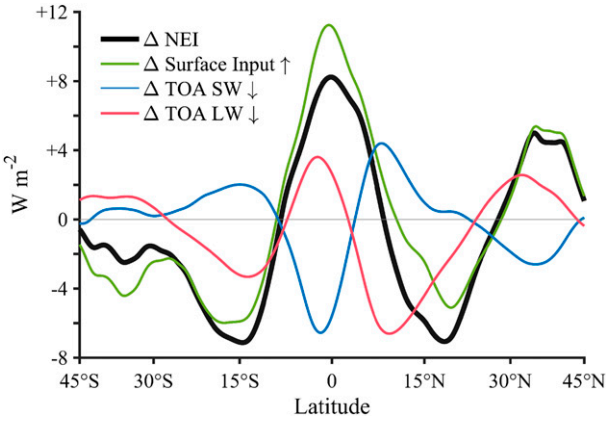

FIG. 7. JFM net energy input difference (ΔNEI) between typical El Niño and La Niña conditions, decomposed into surface energy input (Δsurface input↑, dominated by variations in ocean heat uptake) and net top-of-atmosphere incoming shortwave radiation (ΔTOA SW↓) and outgoing longwave radiation (ΔTOA LW↓). Typical El Niño (La Niña) conditions are defined as ONI values above 0.2 K (below −0.2 K), resulting in a total of 13 El Niño events and 17 La Niña events. Data are taken from ERSST.v3b and ERAI for 1979–2014.

derived from ERAI and NCEP–NCAR (used by D14) reanalyses and ϕ_{med} derived from CMAP (used by D14) and GPCP, as well as the ERAI and NCEP–NCAR precipitation data (Table 2). These correlations indicate that the differences between our results and those of D14 are due to the differences between the AET $\langle[vh]\rangle_0$ in the ERAI and NCEP–NCAR data; the differences are not due to the precipitation datasets.

Since the efficiency of energy transport by the circulation (i.e., the gross moist stability) in the tropics is constrained by local surface conditions (e.g., Held 2001), it is only weakly related to anomalies in cross-equatorial AET, which depend on hemispheric differences in NEI. Differences in AET $\langle[vh]\rangle_0$ among reanalysis datasets therefore primarily arise via dynamical differences in mass transport circulations (Hill et al. 2015). The Hadley cell mass transport is weakest in the NCEP–NCAR reanalysis; in contrast, the ERAI mass transport is close to the ensemble mean of the reanalyses (Nguyen et al. 2013, their Fig. 3). It follows that in the NCEP–NCAR reanalysis, $\langle[vh]\rangle_0$ variations require larger meridional shifts of the tropical circulation, thereby accounting for the increased sensitivity of ϕ_{med} to variations in $\langle[vh]\rangle_0$.

The dependence of the ITCZ latitude indices (ϕ_{NH} for annual and JAS averages and ϕ_{SH} for the JFM averages) on interannual variations in $\langle[vh]\rangle_0$ and $[I_0]$ is shown in Fig. 8. Prominent El Niño and La Niña episodes are highlighted in green and red, respectively. The coefficients of robust univariate regressions (i.e., ITCZ latitude onto either $\langle[vh]\rangle_0$ or $[I_0]$ as predictors) and bivariate regressions (i.e., ITCZ latitude onto both $\langle[vh]\rangle_0$ and $[I_0]$ as predictors) and respective R^2 values are shown in Table 3. The regressions are consistent with Eqs. (5a)–(5b) for annual, JAS, and JFM averages, but the statistical significance is poor because of the relatively small interannual variations. The equatorward (poleward) ITCZ shift in response to warm (cold) ENSO anomalies is evident during all seasons. However, the increase (decrease) in $[I_0]$ in response to warm (cold) ENSO anomalies is clear only during JFM. Similar regressions for ϕ_{med} are found to have a similar dependence on $\langle[vh]\rangle_0$ and $[I_0]$.

Since the ITCZ position is proportional to the ratio of $\langle[vh]\rangle_0$ and $[I_0]$, univariate regressions of the ITCZ position onto either $\langle[vh]\rangle_0$ or $[I_0]$ differ from bivariate regression onto both simultaneously because $\langle[vh]\rangle_0$ and $[I_0]$ covary. Since $\langle[vh]\rangle_0$ changes sign between seasons, the univariate regression coefficients of the ITCZ position onto $[I_0]$ change sign between seasons.

5. Discussion and summary

The zonal-mean ITCZ, defined as the precipitation maximum, lies at the ascending branch of the Hadley circulation, close to where the near-surface meridional mass flux vanishes. It also lies close to the EFE, where the column-integrated meridional atmospheric energy transport vanishes (Figs. 3 and 4). The zonal-mean ITCZ and EFE covary on time scales of seasons and longer, but EFE variations are not exactly in phase with ITCZ variations on seasonal time scales and only capture some aspects of the seasonal ITCZ shifts (Fig. 5), as was already found by Chiang and Friedman (2012).

By expanding the energy flux around the equator, the EFE and thus the ITCZ position can be related to AET

TABLE 2. The Pearson coefficient R of interannual correlations of the annual means of the precipitation median ϕ_{med} and cross-equatorial atmospheric energy transport $\langle[vh]\rangle_0$ for all combinations of the ERAI and NCEP–NCAR reanalyses and GPCP and CMAP precipitation datasets, for 1979–2009. Statistically significant ($p < 0.05$) correlations are highlighted in boldface.

$R(\langle[vh]\rangle_0, \phi_{\text{med}})$		Precipitation dataset			
		ERAI	NCEP–NCAR	GPCP	CMAP
Reanalysis	ERAI	−0.26	−0.28	−0.16	−0.17
	NCEP–NCAR	**−0.65**	**−0.68**	**−0.60**	**−0.66**

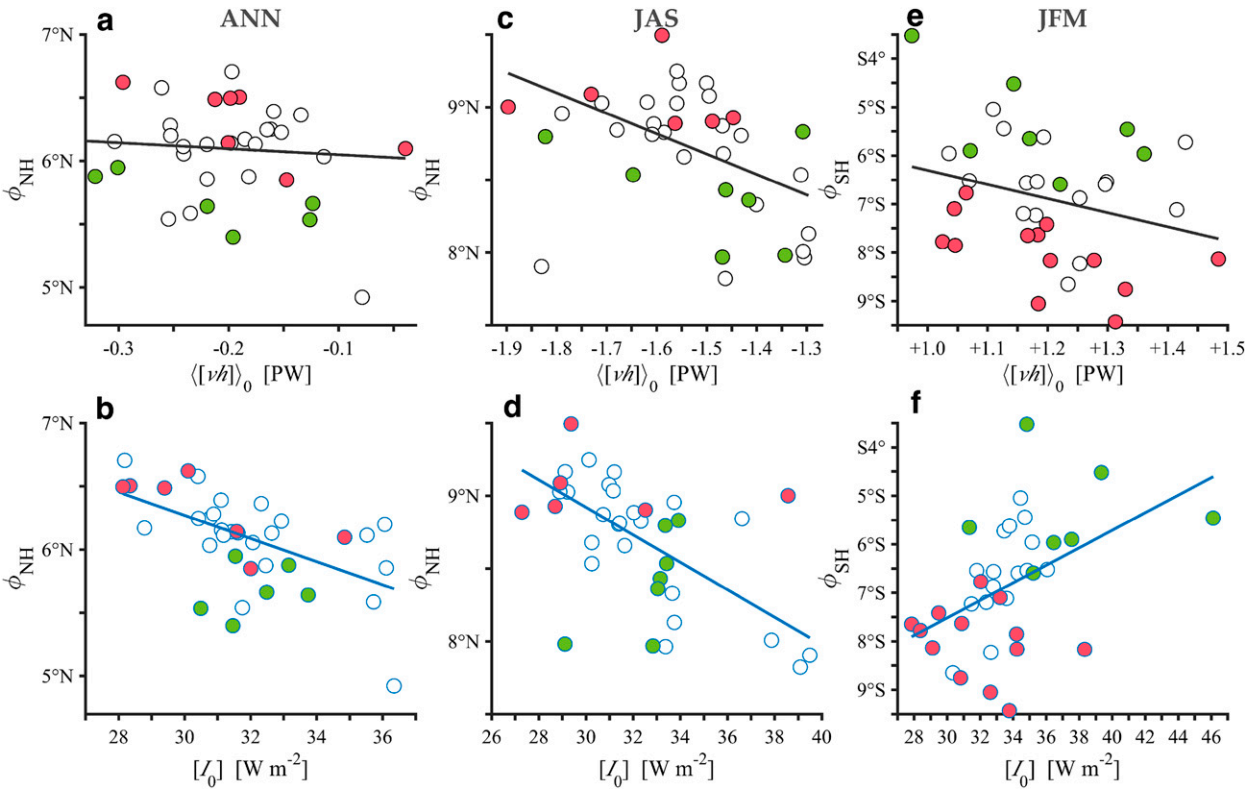

FIG. 8. Dependence of the ITCZ latitude (ϕ_{NH} for ANN and JAS means and ϕ_{SH} for JFM means) on (a),(c),(e) cross-equatorial AET $\langle[vh]\rangle_0$ and (b),(d),(f) equatorial NEI $[I_0]$. Robust linear regressions are shown by solid lines (regression statistics are summarized in Table 3). Prominent El Niño (ONI > 0.5 K; green-filled circles) and La Niña (ONI < −0.5 K; red-filled circles) episodes are highlighted. Data are taken from ERSST.v3b and ERAI for 1979–2014.

and the NEI. To first order, the ITCZ position is proportional to the AET and inversely proportional to NEI near the equator [Eqs. (5a)–(5b)]. This first-order approximation captures the latitude of the climatological mean EFE and its seasonal and interannual variations (Figs. 5 and 6; Tables 1 and 3), providing insight onto the drivers of EFE variations, and thus ITCZ variations. The following key points emerge:

1) Seasonal ITCZ shifts are driven by interhemispheric solar heating differences and are therefore primarily related to the cross-equatorial AET (D13). However, since equatorial NEI peaks at the equinoxes, the ratio of the cross-equatorial AET and equatorial NEI captures the swift transition of the ITCZ across the equator during transition seasons (Fig. 5).
2) Interannual ITCZ migrations are additionally driven by ENSO, which modulates NEI via decreased (increased) ocean heat uptake associated with warm (cold) anomalies—most prominently during boreal winter (Fig. 7).
3) Since the EFE is proportional to the ratio of cross-equatorial AET and NEI and since both quantities exhibit seasonal and interannual variations (Figs. 5, 6, and 8; Table 3), univariate regressions of the ITCZ latitude onto either quantity have limited predictive value. Bivariate regressions of the ITCZ latitude onto both AET and NEI simultaneously perform better.

TABLE 3. The coefficients and respective R^2 of the robust linear regressions of the interannual dependence of the ITCZ position on cross-equatorial AET $\langle[vh]\rangle_0$ and equatorial atmospheric NEI $[I_0]$ (shown in Fig. 8) for ANN, JAS, and JFM means. The coefficients of both univariate regressions (i.e., of ITCZ position on either $\langle[vh]\rangle_0$ or $[I_0]$ as predictors; first and third row for each season) and bivariate regressions (i.e., of ITCZ position on both $\langle[vh]\rangle_0$ and $[I_0]$ as predictors; center row for each season) are shown. Statistically significant ($p < 0.05$) correlations are highlighted in boldface. Data are taken from ERAI for 1979–2014.

	Model coefficients: $\phi = \alpha_0 + \alpha_1\langle[vh]\rangle_0 + \alpha_2[I_0]$			
	α_0 (° lat)	α_1 (° lat PW^{-1})	α_2 (° lat m^2 W^{-1})	R^2
ANN	6.0 ± 0.4	−0.47 ± 2.0	—	0.15
	9.0 ± 1.6	−1.1 ± 1.7	−0.098 ± 0.050	**0.36**
	9.0 ± 1.5	—	−0.091 ± 0.048	**0.31**
JAS	6.6 ± 1.3	−1.4 ± 0.9	—	**0.25**
	9.4 ± 1.4	−1.4 ± 0.7	−0.089 ± 0.035	**0.53**
	12.0 ± 1.3	—	−0.094 ± 0.041	**0.39**
JFM	−3.4 ± 4.6	−2.9 ± 3.8	—	**0.07**
	−9.8 ± 5.7	−2.7 ± 3.3	0.18 ± 0.12	**0.27**
	−13.0 ± 4.1	—	0.18 ± 0.12	**0.21**

The applicability of the EFE framework for understanding the ITCZ position is limited by the possible deviations between the EFE and the ITCZ and by uncertainty in observed TOA and surface budgets (Trenberth et al. 2001). Further testing of the EFE framework in various observational datasets and simulated climates is required. For example, idealized simulations show that as the asymmetry between winter and summer Hadley cells increases with decreasing ocean mixed layer depth, so does the discrepancy between the position of the ITCZ and EFE (D13). In addition, the sensitivity of the ITCZ position to variations in equatorial AET differs between reanalysis datasets (Table 2).

It remains to be tested whether an extension of the EFE framework can account for zonal variations of the ITCZ position and for features such as the bifurcation of the ITCZ to a double ITCZ that straddles the equator in the eastern Pacific during boreal spring (Fig. 1; Zhang 2001; Gu et al. 2005). Results of the corresponding analyses will be presented in Part II of this study.

Acknowledgments. We thank Momme Hell for his visualization advice.

REFERENCES

Adler, R. F., and Coauthors, 2003: The Version-2 Global Precipitation Climatology Project (GPCP) monthly precipitation analysis (1979–present). *J. Hydrometeor.*, **4**, 1147–1167, doi:10.1175/1525-7541(2003)004<1147:TVGPCP>2.0.CO;2.

Bischoff, T., and T. Schneider, 2014: Energetic constraints on the position of the intertropical convergence zone. *J. Climate*, **27**, 4937–4951, doi:10.1175/JCLI-D-13-00650.1.

——, and ——, 2016: The equatorial energy balance, ITCZ position, and double ITCZ bifurcations. *J. Climate*, **29**, 2997–3013, doi:10.1175/JCLI-D-15-0328.1.

Broccoli, A. J., K. A. Dahl, and R. J. Stouffer, 2006: Response of the ITCZ to Northern Hemisphere cooling. *Geophys. Res. Lett.*, **33**, L01702, doi:10.1029/2005GL024546.

Chiang, J. C. H., and C. M. Bitz, 2005: Influence of high latitude ice cover on the marine intertropical convergence zone. *Climate Dyn.*, **25**, 477–496, doi:10.1007/s00382-005-0040-5.

——, and A. R. Friedman, 2012: Extratropical cooling, interhemispheric thermal gradients, and tropical climate change. *Annu. Rev. Earth Planet. Sci.*, **40**, 383–412, doi:10.1146/annurev-earth-042711-105545.

Curry, J., C. Clayson, W. Rossow, R. Reeder, Y.-C. Zhang, P. Webster, G. Liu, and R.-S. Sheu, 1999: High-resolution satellite-derived dataset of the surface fluxes of heat, freshwater, and momentum for the TOGA COARE IOP. *Bull. Amer. Meteor. Soc.*, **80**, 2059–2080, doi:10.1175/1520-0477(1999)080<2059:HRSDDO>2.0.CO;2.

Dai, A., and T. M. L. Wigley, 2000: Global patterns of ENSO-induced precipitation. *Geophys. Res. Lett.*, **27**, 1283–1286, doi:10.1029/1999GL011140.

Dee, D. P., and S. Uppala, 2009: Variational bias correction of satellite radiance data in the ERA-Interim reanalysis. *Quart. J. Roy. Meteor. Soc.*, **135**, 1830–1841, doi:10.1002/qj.493.

——, and Coauthors, 2011: The ERA-Interim reanalysis: Configuration and performance of the data assimilation system. *Quart. J. Roy. Meteor. Soc.*, **137**, 553–597, doi:10.1002/qj.828.

Donohoe, A., J. Marshall, D. Ferreira, and D. McGee, 2013: The relationship between ITCZ location and cross-equatorial atmospheric heat transport: From the seasonal cycle to the last glacial maximum. *J. Climate*, **26**, 3597–3618, doi:10.1175/JCLI-D-12-00467.1.

——, ——, ——, K. Armour, and D. McGee, 2014: The interannual variability of tropical precipitation and interhemispheric energy transport. *J. Climate*, **27**, 3377–3392, doi:10.1175/JCLI-D-13-00499.1.

Fasullo, J. T., and K. E. Trenberth, 2008: The annual cycle of the energy budget. Part II: Meridional structures and poleward transports. *J. Climate*, **21**, 2313–2325, doi:10.1175/2007JCLI1936.1.

Frierson, D. M. W., and Y.-T. Hwang, 2012: Extratropical influence on ITCZ shifts in slab ocean simulations of global warming. *J. Climate*, **25**, 720–733, doi:10.1175/JCLI-D-11-00116.1.

——, and Coauthors, 2013: Contribution of ocean overturning circulation to tropical rainfall peak in the Northern Hemisphere. *Nat. Geosci.*, **6**, 940–944, doi:10.1038/ngeo1987.

Gu, G., R. Adler, and A. Sobel, 2005: The eastern Pacific ITCZ during the boreal spring. *J. Atmos. Sci.*, **62**, 1157–1174, doi:10.1175/JAS3402.1.

Held, I. M., 2001: The partitioning of the poleward energy transport between the tropical ocean and atmosphere. *J. Atmos. Sci.*, **58**, 943–948, doi:10.1175/1520-0469(2001)058<0943:TPOTPE>2.0.CO;2.

Hill, S. A., Y. Ming, and I. M. Held, 2015: Mechanisms of forced tropical meridional energy flux change. *J. Climate*, **28**, 1725–1742, doi:10.1175/JCLI-D-14-00165.1.

Kalnay, E., and Coauthors, 1996: The NCEP/NCAR 40-Year Reanalysis Project. *Bull. Amer. Meteor. Soc.*, **77**, 437–471, doi:10.1175/1520-0477(1996)077<0437:TNYRP>2.0.CO;2.

Kang, S. M., I. M. Held, D. M. W. Frierson, and M. Zhao, 2008: The response of the ITCZ to extratropical thermal forcing: Idealized slab-ocean experiments with a GCM. *J. Climate*, **21**, 3521–3532, doi:10.1175/2007JCLI2146.1.

——, D. M. W. Frierson, and I. M. Held, 2009: The tropical response to extratropical thermal forcing in an idealized GCM: The importance of radiative feedbacks and convective parameterization. *J. Atmos. Sci.*, **66**, 2812–2827, doi:10.1175/2009JAS2924.1.

Liu, Z., D. Ostrenga, W. Teng, and S. Kempler, 2012: Tropical Rainfall Measuring Mission (TRMM) precipitation data and services for research and applications. *Bull. Amer. Meteor. Soc.*, **93**, 1317–1325, doi:10.1175/BAMS-D-11-00152.1.

Marshall, J., A. Donohoe, D. Ferreira, and D. McGee, 2014: The ocean's role in setting the mean position of the inter-tropical convergence zone. *Climate Dyn.*, **42**, 1967–1979, doi:10.1007/s00382-013-1767-z.

Neelin, J. D., and I. M. Held, 1987: Modeling tropical convergence based on the moist static energy budget. *Mon. Wea. Rev.*, **115**, 3–12, doi:10.1175/1520-0493(1987)115<0003:MTCBOT>2.0.CO;2.

Nguyen, H., A. Evans, C. Lucas, I. Smith, and B. Timbal, 2013: The Hadley circulation in reanalyses: Climatology, variability, and change. *J. Climate*, **26**, 3357–3376, doi:10.1175/JCLI-D-12-00224.1.

Peixoto, J. P., and A. H. Oort, 1992: *Physics of Climate*. American Institute of Physics, 555 pp.

Poli, P., S. Healy, and D. Dee, 2010: Assimilation of global positioning system radio occultation data in the ECMWF ERA-Interim reanalysis. *Quart. J. Roy. Meteor. Soc.*, **136**, 1972–1990, doi:10.1002/qj.722.

Reichler, T., M. Dameris, and R. Sausen, 2003: Determining the tropopause height from gridded data. *Geophys. Res. Lett.*, **30**, 2042, doi:10.1029/2003GL018240.

Schneider, T., T. Bischoff, and G. H. Haug, 2014: Migrations and dynamics of the intertropical convergence zone. *Nature*, **513**, 45–53, doi:10.1038/nature13636.

Smith, T., R. Reynolds, T. Peterson, and J. Lawrimore, 2008: Improvements to NOAA's historical merged land–ocean surface temperature analysis (1880–2006). *J. Climate*, **21**, 2283–2296, doi:10.1175/2007JCLI2100.1.

Trenberth, K. E., 1997: Using atmospheric budgets as a constraint on surface fluxes. *J. Climate*, **10**, 2796–2809, doi:10.1175/1520-0442(1997)010<2796:UABAAC>2.0.CO;2.

——, J. M. Caron, and D. P. Stepaniak, 2001: The atmospheric energy budget and implications for surface fluxes and ocean heat transports. *Climate Dyn.*, **17**, 259–276, doi:10.1007/PL00007927.

Wielicki, B. A., B. Barkstrom, E. Harrison, R. Lee, G. Smith, and J. Cooper, 1996: Clouds and the Earth's Radiant Energy System (CERES): An Earth observing system experiment. *Bull. Amer. Meteor. Soc.*, **77**, 853–868, doi:10.1175/1520-0477(1996)077<0853:CATERE>2.0.CO;2.

Xie, P., and P. Arkin, 1996: Analyses of global monthly precipitation using gauge observations, satellite estimates, and numerical model predictions. *J. Climate*, **9**, 840–858, doi:10.1175/1520-0442(1996)009<0840:AOGMPU>2.0.CO;2.

Yan, H., W. Wei, W. Soon, Z. An, W. Zhou, Z. Liu, Y. Wang, and R. Carter, 2015: Dynamics of the intertropical convergence zone over the western Pacific during the Little Ice Age. *Nat. Geosci.*, **8**, 315–320, doi:10.1038/ngeo2375.

Yoshimori, M., and A. J. Broccoli, 2008: Equilibrium response of an atmosphere–mixed layer ocean model to different radiative forcing agents: Global and zonal mean response. *J. Climate*, **21**, 4399–4423, doi:10.1175/2008JCLI2172.1.

Zhang, C., 2001: Double ITCZs. *J. Geophys. Res.*, **106**, 11 785–11 792, doi:10.1029/2001JD900046.